SUPPLEMENTARY INFORMATION

Supplementary Information for "Superconducting quantum circuits at the surface code threshold for fault tolerance"

R. Barends,[1, *] J. Kelly,[1, *] A. Megrant,[1] A. Veitia,[2] D. Sank,[1] E. Jeffrey,[1] T. C. White,[1] J. Mutus,[1] A. G. Fowler,[1, 3] B. Campbell,[1] Y. Chen,[1] Z. Chen,[1] B. Chiaro,[1] A. Dunsworth,[1] C. Neill,[1] P. O'Malley,[1] P. Roushan,[1] A. Vainsencher,[1] J. Wenner,[1] A. N. Korotkov,[2] A. N. Cleland,[1] and John M. Martinis[1]

[1]*Department of Physics, University of California, Santa Barbara, CA 93106, USA*
[2]*Department of Electrical Engineering, University of California, Riverside, CA 92521, USA*
[3]*Centre for Quantum Computation and Communication Technology,*
School of Physics, The University of Melbourne, Victoria 3010, Australia

DEVICE FUNDAMENTALS

Fabrication

The devices are made in a process similar to the fabrication steps outlined in Ref. [1], with an important improvement: we have added crossovers to suppress stray microwave chip modes by tying the ground planes together with low impedance connections. Otherwise, the many control wires in our chip could lead to segmentation of the ground plane, and the appearance of parasitic slotline modes [2]. The device is made in a five-step deposition process, (I) Al deposition and control wiring etch, (II) crossover dielectric deposition, (III) crossover Al deposition, (IV) Qubit capacitor and resonator etch, (V) Josephson junction deposition. The qubit capacitor, ground plane, readout resonators, and control wiring are made using molecular beam epitaxy (MBE)-grown Al on sapphire [3]. The control wiring is patterned using lithography and etching with a BCl_3/Cl_2 reactive ion etch. A 200 nm thick layer of SiO_2 for the crossover dielectric is deposited in an e-beam evaporator, followed by lift-off. We fabricate crossovers on all the control wiring, using a SiO_2 dielectric that has a non-negligible loss tangent. An in-situ Ar ion mill is used to remove the native AlO_x insulator, after which a 200 nm Al layer for the crossover wiring is deposited in an e-beam evaporator, followed by lift-off. We used 0.9 μm i-line photoresist, lift-off is done in N-methyl-2-pyrrolidone at 80°C. A second BCl_3/Cl_2 etch is used to define the qubit capacitor and resonators; this step is separate from the wiring etch to prevent the sensitive capacitor from seeing extra processing. Lastly, we use electron beam lithography, an in-situ Ar ion mill, and double angle shadow evaporation to deposit the Josephson junctions, in a final lift-off process. See Ref. [1] for details.

Coherence Times

Energy relaxation times T_1 of all qubits are shown in Fig. S1, measured over a frequency range from 4 to 6 GHz. We find typical T_1 values between 20 and 40 μs. Variations in T_1 arise predominantly from the qubit interacting incoherently with weakly coupled two-level defects, as discussed in Ref. [1]. In this previous work we found that larger area (with longer and wider legs) Xmon qubits showed higher T_1 values as well as large, frequency-specific suppressions in the energy coherence: for certain frequencies the T_1 would decrease to values below 10 μs. We attribute these large suppressions to chip modes, arising from imbalances in the microwave control lines, to which the larger Xmon geometries can couple more strongly. The data in Fig. S1 exhibit fewer of such suppressions; we believe that this improvement is due to the addition of crossovers.

We have investigated the Ramsey dephasing times versus frequency for qubit Q_1. The Ramsey decay envelope is measured by phase tomography (see Ref. [1]) and fitted to the function $\exp[-t/T_{\phi,1} - (t/T_{\phi,2})^2]$. Fast dephasing, from white noise as well as energy relaxation, is captured in $T_{\phi,1}$, and slow, Gaussian dephasing is captured in $T_{\phi,2}$. Typical dephasing times are plotted in Fig. S2. We find a fast dephasing time on the order of 10 μs; this value is below the energy coherence time, and may be due to white noise from the room temperature control electronics. The slow, Gaussian dephasing times are consistent with a $1/f$-spectrum with a spectral density of $S_\Phi(1 \text{ Hz}) = 1.1 \, \mu\Phi_0/\sqrt{\text{Hz}}$.

Qubit Frequencies and Coupling

Qubit frequencies and nearest neighbour coupling strengths are listed in Table S1.

TABLE S1: Qubit frequencies and nonlinearities ($f_{21} - f_{10}$) at the zero flux bias (degeneracy point) and coupling strengths in MHz. The coupling strength is measured at frequencies between 4.2 and 4.7 GHz. We find a typical next-nearest neighbour coupling of $g/2\pi = 1.3$ MHz, consistent with microwave circuit simulations.

qubits	Q_0	Q_1	Q_2	Q_3	Q_4
f_{10}	5805	5238	5780	5060	5696
nonlinearity	-217	-226	-214	-212	-223
$g_{01}/2\pi$ (4.22 GHz)	27.7				
$g_{12}/2\pi$ (4.70 GHz)		30.8			
$g_{23}/2\pi$ (4.66 GHz)			30.4		
$g_{34}/2\pi$ (4.65 GHz)				30.9	

Z Crosstalk

We measure a crosstalk between the frequency Z control lines and qubits that is small, approximately $1-2\%$. After adding
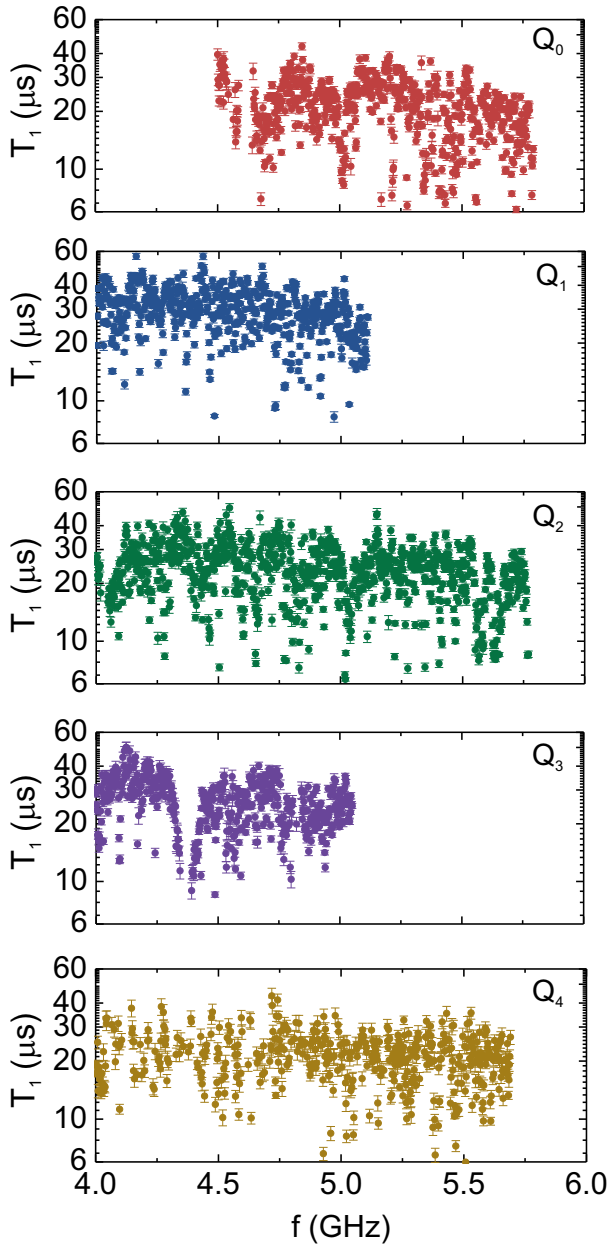

FIG. S1: **Energy Relaxation for Xmon Qubits.** Frequency dependence of T_1 for all qubits. The frequency step size is 2 MHz. The values for T_1 are generally in the 20-40 μs range, we find T_1 values up to 57 μs. The depression at 4.36 GHz in qubit Q_3 is due to a coherently coupled junction defect.
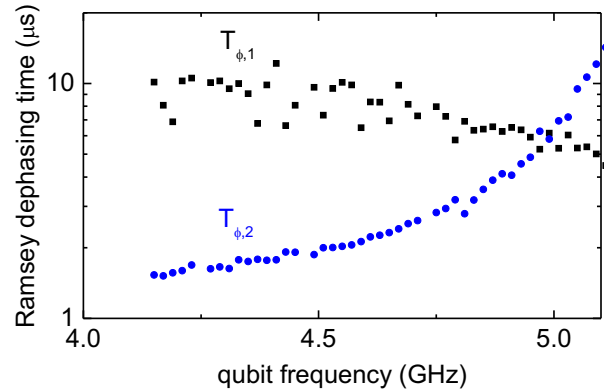

FIG. S2: **Ramsey dephasing.** Frequency dependence of the fast ($T_{\phi,1}$) and slow ($T_{\phi,2}$) Ramsey dephasing times of qubit Q_1. Flux bias points Φ/Φ_0 range from 0.1 to 0.28, and $\delta f_{10}/\delta(\Phi/\Phi_0)$ range from -16 to -50 GHz.

compensation pulses to orthonormalise the control, we find a remnant crosstalk of below 10^{-4}. The crosstalk matrix M_Φ is shown below, defined as: $\Phi_{\text{actual}} = M_\Phi\Phi_{\text{ideal}}$, with Φ the flux threaded through each qubit's superconducting quantum interference device (SQUID) loop.

$$M_\Phi = \begin{pmatrix} 1.000 & -0.023 & -0.014 & -0.009 & -0.006 \\ 0.019 & 1.000 & -0.022 & -0.011 & -0.007 \\ 0.017 & 0.000 & 1.000 & -0.016 & -0.009 \\ 0.016 & 0.008 & -0.015 & 1.000 & -0.014 \\ 0.013 & 0.014 & -0.016 & -0.010 & 1.000 \end{pmatrix}$$

EXPERIMENTAL SETUP

The wiring diagram and circuit components are shown in Fig. S3.

FLATTENING THE Z RESPONSE

Imperfections in the frequency control wiring can cause ripples after a pulse. Left unchecked, these can affect gate fidelity significantly, appearing as single qubit phase errors, see Fig. S4. We employ a two-step procedure to correct for these non-idealities. We first calibrate the room temperature electronics by measuring the unit step (Heaviside step) response at the output of the Z control board.

With the board response corrected by deconvolution, we measure the qubit phase as a function of time $\Delta\tau$ after the end of a unit step. This probes the transfer function of the fridge wiring, contact pads and on-chip control lines. When no unit step is applied, the X/2 pulse rotates the qubit state onto the Y axis. When applying a unit step, deviations in frequency will cause
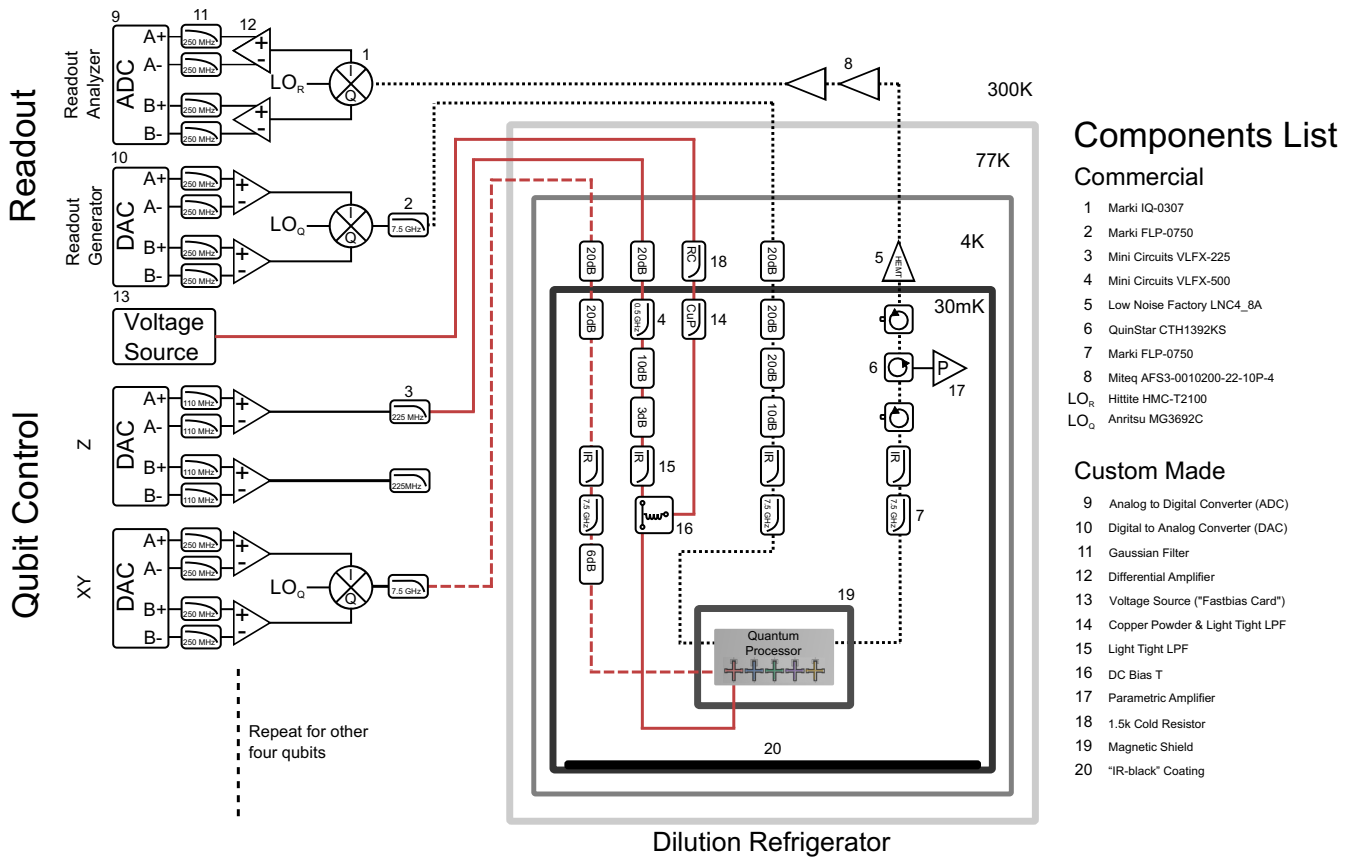
FIG. S3: Electronics and Control Wiring. Diagram detailing all of the control electronics, control wiring, and filtering for the experimental setup. Each qubit uses one digital to analog converter (DAC) channel for each of the X, Y, and Z rotations. Additionally, we use a DC bias tee to connect a voltage source to each qubit frequency control line to give a static frequency offset. All five qubits are read out using frequency-domain multiplexing on a single measurement line. The readout DAC generates five measurement tones at the distinct frequencies corresponding to each qubit's readout resonator. The signal is amplified by a wideband parametric amplifier [4], a high electron mobility transistor (HEMT), and room temperature amplifiers before demodulation and state discrimination by the analog to digital converter (ADC). All control wires go through various stages of attenuation and filtering to prevent unwanted signals from disturbing the quantum processor. Two local oscillators (LO_Q) are used for qubit XY control, at 4.5 and 5.6 GHz. The readout LO_R is at 6.76 GHz. All LO, DAC, and ADC electronics are locked to a 10 MHz SRS FS725 rubidium frequency standard.

the Bloch sphere vector to deviate from the Y axis. A subsequent Y/2 pulse will make this apparent in the measured excited state probability. We note that this measurement is first order sensitive to small deviations – the difference in probability denotes the phase deviation ($\Delta\phi \approx \Delta P_{|1\rangle}$) – whereas Ramsey and quantum state tomography are second order sensitive: The $\pi/2$ pulses used in tomography project the state onto the Z axis, thus the reconstruction of the phase or state is done from probabilities ($P \approx 1 - \Delta\phi^2/2$) which are second order sensitive to ϕ.

We find that the transfer function can be described by an exponential response with two timescales. Typical values are 100 ns and 5 ns. The longer timescale is consistent with the L/R time arising from the bias tee, with $L \approx 6~\mu H$ and $R = 50~\Omega$. We believe that the short timescale arises from reflections. The impulse response of an imperfect wire

with reflection r, placed time T away from the wire's end is $H(\omega) = 1 - r + \sum_{k=1}^{\infty} r^k \exp(-2ik\omega T)$; at low frequencies this can be approximated by the impulse response function $h(t) \propto \exp(-t/2rT)u(t)$. Assuming reflection coefficients on the order of -10 dB and round trip times $2T$ between qubit and mixing plate electronics on the order several ns, the effective decay time $2rT$ is on the order of a few ns.

With the corrections in place, by deconvolving both the board response and fridge wiring, remnant control pulse ripples are suppressed to below 10^{-4}: We find qubit phase deviations consistent with a 30 kHz drift after applying a 0.5 GHz detuning step pulse, see Fig. S4. The calibrations discussed above are key for obtaining accurate CZ gates [5].
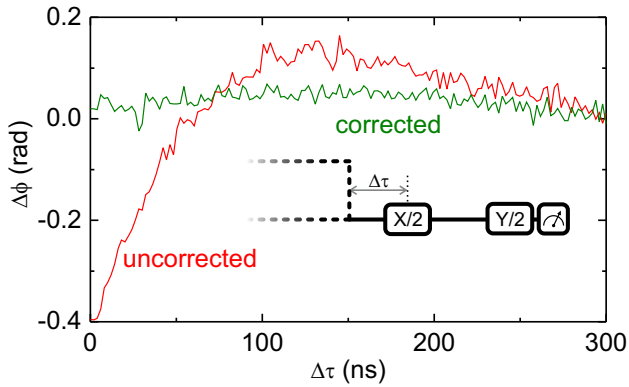
FIG. S4: **Control pulse ripple.** Qubit phase response to a unit step (amplitude: 0.5 GHz) applied to the frequency control line, with and without correction. The pulse sequence is shown in the inset, with the dashed line representing the unit step. With correction, a phase drift of 0.03 rad in 150 ns is observed, consistent with a remnant control pulse ripple of 30 kHz.

SINGLE QUBIT AND TWO-QUBIT GATE FIDELITIES OF ALL QUBITS

A comprehensive listing of all single qubit gate fidelities of all qubits is shown in Table S2, the gate durations are in Table S3. A listing of all CZ gate fidelities can be found in Table S4.

SCALING UP THE ARCHITECTURE

In the present experiment, we have demonstrated single- and two-qubit gates at the surface code threshold in a one-dimensional array with five Xmon qubits. Scaling up to a larger one-dimensional array is trivial by adding more qubits on the sides. For scaling up to a two-dimensional grid, we envision an approach with Xmon qubits placed in a square lattice, capacitively coupled to their four nearest neighbours. The Xmon qubit, with the four arms available for coupling, has been designed with this task in mind. The qubits are placed in one layer, and in the envisioned approach control and readout are placed on other planes. Methods to connect these planes are known: Bump bonds and vias allow for making galvanic connections between multiple layers, and capacitive coupling between planes is made easy by the presence of a dielectric substrate. While this approach is conceptually straightforward, the required microfabrication technology will need to be developed further. A schematic of the proposed approach is shown in Fig. S5.

While it is straightforward to lithographically define more qubits on a chip, the crucial challenge in scaling up to a two-dimensional array – with added wiring and readout – is to maintain the high coherence and gate fidelity, without sacrificing addressability of individual qubits. We believe that this will guide the approach to and the development of the required microfab-

rication. We are optimistic about scaling up, as coherence was maintained in moving from isolated qubits (in Ref. [1]) to the one-dimensional array here.

TABLE S2: Single qubit gate fidelities for all qubits, determined by Clifford-based randomised benchmarking. Averaged over all gates and all qubits we find an average fidelity of 0.9992. The standard deviation is typically $5 \cdot 10^{-5}$. The gate times are between 10 and 20 ns, see Table S3, except for the composite gates H and 2T, which are twice as long. The idle is as long as the shortest microwave gate (12 ns to 20 ns).

gates	Q_0	Q_1	Q_2	Q_3	Q_4
I	0.9990	0.9996	0.9995	0.9994	0.9991
X	0.9992	0.9996	0.9992	0.9991	0.9991
Y	0.9991	0.9995	0.9993	0.9992	0.9991
X/2	0.9992	0.9993	0.9993	0.9994	0.9993
Y/2	0.9991	0.9993	0.9995	0.9994	0.9994
-X	0.9991	0.9995	0.9992	0.9989	0.9991
-Y	0.9991	0.9995	0.9991	0.9987	0.9991
-X/2	0.9991	0.9992	0.9993	0.9990	0.9995
-Y/2	0.9991	0.9992	0.9995	0.9990	0.9994
H	0.9986	0.9986	0.9991	0.9981	0.9988
Z	0.9995	0.9988	0.9994	0.9991	0.9993
Z/2	0.9998	0.9991	0.9998	0.9995	0.9996
2T ^{a}		0.9989	0.9994	0.9989	0.9990
average over gates	0.9992	0.9992	0.9994	0.9991	0.9992
average over qubits			0.9992		

^{a}As the T gate is not a Clifford generator, the recovery gate is not within the group when interleaving. This precludes Clifford-based randomised benchmarking of the T gate. To quantify this gate to some extent, we have benchmarked 2T gates, physically implemented by applying two T gates in series. If the gate error is predominantly gate-aspecific, the T gate error is half that of the 2T gate, suggesting that the average T gate fidelity is 0.9995

TABLE S3: Single qubit gate times in ns.

gates	Q_0	Q_1	Q_2	Q_3	Q_4
XY axes π rotations	20	20	12	18	12
XY axes $\pi/2$ rotations	20	20	12	12	12
Z axis $\pi, \pi/2, \pi/4$ rotations	10	10	10	10	10
I	20	20	12	12	12
H	40	40	24	30	24
2T	20	20	20	20	20

TABLE S4: CZ gate fidelities for all qubit pairs, determined by Clifford-based randomised benchmarking. Gate times are between 38 and 45 ns; Q_0-Q_1: 45 ns, Q_1-Q_2: 43 ns, Q_2-Q_3: 43 ns, Q_3-Q_4: 38 ns.

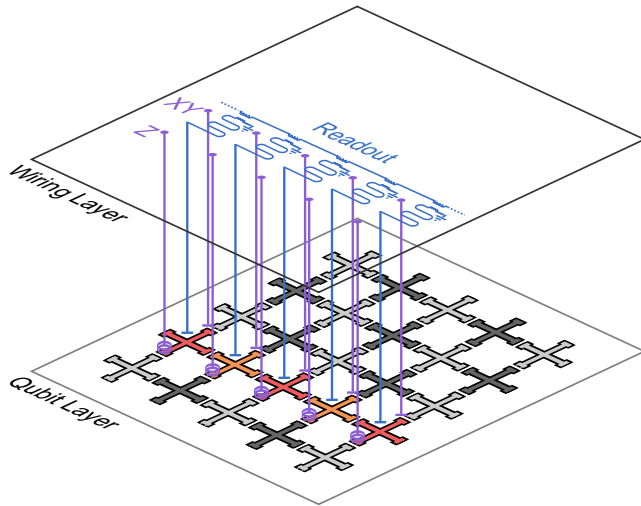| qubits	Q_0	Q_1	Q_2	Q_3	Q_4
$CZ_{Q_0-Q_1}$	0.9924 $\pm$ 0.0005				
$CZ_{Q_1-Q_2}$		0.9936 $\pm$ 0.0004			
$CZ_{Q_2-Q_3}$			0.9944 $\pm$ 0.0005		
$CZ_{Q_3-Q_4}$				0.9900 $\pm$ 0.0006	

FIG. S5: **Schematic of the proposed approach to scaling up.** The Xmon qubits are placed in a checkerboard pattern in a single layer, with data qubits (light) and measurement qubits (dark). Control, readout, and wiring are placed in other layers; connections between the layers are made by capacitive coupling, and by bump bonds and vias for galvanic connections. The row with the five Xmon qubits coloured red and orange is the experiment we have implemented (see Fig. 1 in the main Letter), and can clearly be seen as a building block for the two-dimensional array.

FIG. S6: **CZ error budget.** (a) In the Ramsey error filter technique an interference pattern arises in the measured probability (black dots) whose magnitude is proportional to the $|02\rangle$-state leakage. The data are smoothed (red) for enhanced visibility. The frequency of these oscillations (indicated by the arrow, 1.6 ns) is the idling frequency difference between qubits (800 MHz), minus the nonlinearity (200 MHz) as we are measuring the crossing between $|11\rangle$ and $|02\rangle$. Other frequencies are believed to arise from improper $|11\rangle$ state preparation. (b) Randomised benchmarking sequence fidelity for qubits Q_2 and Q_3. Decoherence is quantified by idling for the same duration as the CZ gate. Controls error can be identified by applying the control pulse on Q_2, without doing a full CZ by detuning Q_3. For the randomised benchmarking data of the CZ (not shown): $r_{\rm ref} = 0.0198$ and $r_{\rm CZ} = 0.0269$.

VERIFYING EXPERIMENTAL FIDELITIES ARE AT THE SURFACE CODE THRESHOLD

We shall simulate inceasing size versions of Fig. S5. Note that the single-qubit and two-qubit gate physics is identical in this architecture, justifying the use of the reported experimental fidelities. One additional feature in 2-D is the need to use a periodic array of frequencies, leading to interactions between qubits with the same frequencies and driving of the entire set of qubits with a given frequency when any given qubit is manipulated. The magnitude of the interactions and driving crosstalk will only decay quadratically with qubit separation.

We have simulated these crosstalk effects in detail and have found them to be surprisingly tolerable, as such errors are only two-body correlated at worst, and non-neighbouring, leading to information local to both halves of the error, and efficient correction [6]. We shall therefore neglect crosstalk in the simulations of the section to focus the analysis on the fidelity of the reported gates.

Nominally, the threshold fidelity of the surface code is 0.99 [7], provided one assumes there is no leakage, the two-qubit interaction is the dominant source of error, and gates can be performed perfectly in parallel. The physical device described in this work has complex behavior outside these assumptions, necessitating a device-specific calculation of the surface code threshold fidelity.

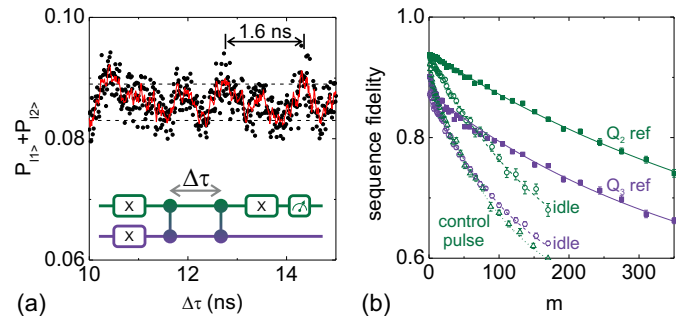When a CZ gate is applied, no qubit neighbouring either of the qubits involved in the CZ can be involved in their own CZ gate. We have devised a 16 step CZ application pattern that accounts for these parallelism constraints and still measures all stabilizers. The longest measured CZ time of 45 ns will be used. Furthermore, the CZ gate, which is always applied between one measurement qubit and one data qubit, has a small amount of leakage ($< 0.2\%$) on the measurement qubit, but practically negligible leakage on the data qubit. We shall neglect this small amount of measurement qubit leakage. Methods of coping with leakage in topological codes are known [8].

Measurement with fidelity 0.99 in 200 ns and initialization with fidelity 0.99 in 50 ns will be assumed [9]. Y/2 gates will be used instead of Hadamard gates, with the slowest 20 ns time assumed and an average fidelity of 0.9992 (calculated only from the slower Y/2 gates) assumed. An identity error of 0.05% per 10 ns will be assumed, consistent with experimental data.

Detailed simulations of 5x5, 9x9, and 13x13 qubit arrays with the above parameters have been performed making use of the latest correction techniques [10]. The logical error rate was found to be the same in all cases, justifying our claim of a device with parameters at the surface code threshold.

CZ GATE ERROR BUDGET

We experimentally measure the three predominant error mechanisms of the CZ gate: 2-state leakage, decoherence and control error. 2-state leakage is measured using the same technique as outlined in [11]. The system is initialised in the $|11\rangle$-state followed by two CZ gates. As the time between these two

gates is varied, we measure an interference pattern in the probability where the magnitude is proportional to the $|02\rangle$ state leakage, see Fig. S6a. The error is given by $\Delta P/4$, with ΔP the peak-to-peak difference in probability [11]. We also see additional interference patterns that come from imperfect $|11\rangle$ preparation at the beginning of the sequence. We note that leakage occurs predominantly in the qubit which undergoes the frequency trajectory.

We measure the decoherence contribution from each qubit by performing interleaved randomised benchmarking with an idle of the same duration as the CZ gate, see Fig. S6b. The contribution to error from the waveform is measured by interleaved randomised benchmarking on the waveform for the CZ gate alone, with a slightly lower amplitude to avoid interactions with the other qubit. We treat this as a single-qubit phase gate. With the idle error measured, we can separate out decoherence and single qubit phase error. Because we are detuning the qubit down in frequency to a part of the spectrum where it is more sensitive to flux noise, inducing more dephasing, the single qubit phase error is an upper bound. With these experiments we can construct an error budget for all of the dominant error mechanisms, as seen in Table S5.

QUANTIFYING XY CONTROL CROSSTALK USING SIMULTANEOUS RANDOMISED BENCHMARKING

Addressability, the ability to individually control a single qubit without affecting neighbouring qubits, is of great importance when building a multi-qubit system. In our five Xmon qubit processor the addressability is mostly compromised in three ways: Z control crosstalk, microwave XY control crosstalk, and off-resonant qubit-qubit coupling. Z crosstalk can be reduced to below the 10^{-4} level. Microwave XY crosstalk becomes a problem if a qubit's control pulses perform rotations on a neighbouring qubit. Off-resonant qubit-qubit coupling will very slowly perform a CZ gate between the qubits, potentially causing unwanted phase shifts with rate Ω_{ZZ},

$$\Omega_{ZZ} = -\frac{2g^2(\eta_1 + \eta_2)}{(\Delta - \eta_1)(\Delta + \eta_2)}, \tag{S1}$$

with η_1 and η_2 the qubit nonlinearities, and Δ the difference in qubit frequencies.

We performed crosstalk characterisation on nearest neighbour and next-nearest neighbour qubits. Nearest neighbours are far detuned (> 800 MHz), hence the microwave XY crosstalk is
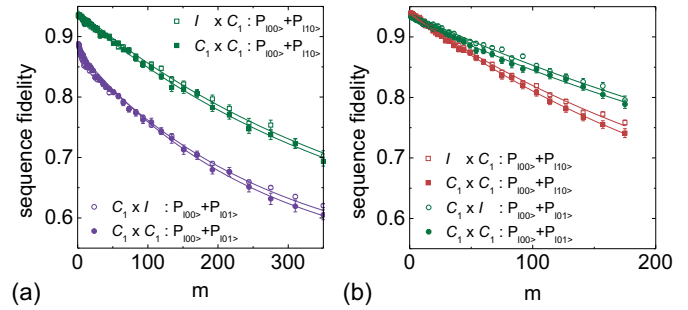

FIG. S7: **Simultaneous randomised benchmarking of nearest and next nearest neighbours.** (a) Benchmarking the effect of Q_2 on Q_3 and vice-versa ($f_{Q_2} = 5.72$ GHz, $f_{Q_3} = 4.67$ GHz). The sequence fidelities are shown for operating Q_2 individually ($I \otimes C_1$, green open squares), Q_3 individually ($C_1 \otimes I$, purple open circles), and Q_2 and Q_3 simultaneously ($C_1 \otimes C_1$, full symbols). By tracing out one qubit, its effect on the other qubit becomes apparent: the errors per Clifford are: $r_{Q2}=0.0011$, $r_{Q2|Q3}=0.0012$, $r_{Q3}=0.0018$, $r_{Q3|Q2}=0.0020$. (b) Benchmarking of Q_0 and Q_2 ($f_{Q_0} = 5.30$ GHz, $f_{Q_2} = 5.72$ GHz). The errors per Clifford are: $r_{Q0}=0.0016$, $r_{Q0|Q2}=0.0018$, $r_{Q2}=0.0011$, $r_{Q2|Q0}=0.0011$. Note that the errors per Clifford are consistent with the average gate fidelities in Table S2: for Q_2, the average gate fidelity is $1 - r_{Q2}/1.875=0.9994$. Coupling strengths can be found in Table S1.

expected to be negligible, but the off-resonant CZ interaction may be non-negligible. Next-nearest neighbors have a much smaller coupling ($g/2\pi = 1.3$ MHz), but are only detuned by 100-400 MHz; hence both the off-resonant CZ as well as microwave XY crosstalk may be detrimental. We investigate these mechanisms by using the simultaneous randomised benchmarking techniques outlined in Ref. [12]. We can single out errors that come from poor addressability by performing randomised benchmarking on each qubit individually, and operating both qubits simultaneously.

The randomised benchmarking data are shown in Fig. S7. We can determine the effect of controlling qubit Q_3 on Q_2, by first benchmarking qubit Q_2 individually ($I \otimes C_1$, green open squares), and benchmarking both qubit Q_2 and Q_3 simultaneously, and tracing out the contribution of Q_3 ($C_1 \otimes C_1$, green full squares). The decay for both traces is virtually indistinguishable, the added error is below 10^{-4}. Likewise, we find that the effect on Q_3 of controlling Q_2 simultaneously leads to an added error per Clifford of $2 \cdot 10^{-4}$. For next nearest neighbours, we find added errors per Clifford of $1 \cdot 10^{-4}$ and $2 \cdot 10^{-4}$. For both the nearest neighbour and next-nearest neighbours the added error per Clifford of operating them simultaneously is $< 2 \cdot 10^{-4}$, the inferred added error per single qubit gate is therefore $< 10^{-4}$. We conclude that XY control crosstalk is a minor error mechanism, enabling a high degree of addressability in this architecture.

TABLE S5: CZ gate error budget, including the contribution to the total error in percent.

Decoherence (55%)	Q_2	≥ 0.0017 (24%)
	Q_3	0.0022 (31%)
Control (45%)	single qubit phase error	≤ 0.0017 (24%)
	state leakage	0.0015 (21%)

GENERATION OF THE CLIFFORD GROUPS

Single qubit Clifford group C_1

The single qubit Clifford group C_1 is the group of 24 rotations which preserve the octahedron in the Bloch sphere. We implement the group using microwave pulses only, decomposed into rotations around the X and Y axes using the generators: {I, $\pm$X/2, $\pm$Y/2, $\pm$X, $\pm$Y}, as summarised in Table S6. The average number of single qubit gates per single qubit Clifford is 1.875.

Two qubit Clifford group C_2

Using the single qubit Cliffords, we can construct the two qubit Clifford group C_2 following Ref. [13]. This group has four classes: the single qubit class, the CNOT-like class, the iSWAP-like class, and the SWAP-like class. The CNOT and SWAP-like class are terminated with a gate from the 3-element group S_1, as described in Table S7. The single qubit class has $24^2 = 576$ elements:
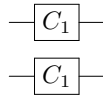

TABLE S6: The 24 single qubit Cliffords written in terms of the physical microwave gates applied in time. The Paulis and $2\pi/3$ rotations form the tetrahedron symmetry group. Here, X/2 denotes a $\pi/2$ rotation over the X axis, with unitary $R_X(\pi/2) = \exp(-i\pi\sigma_X/4)$.

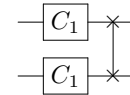| Single qubit Cliffords	
Paulis	I
	X
	Y
	Y,　X
$2\pi/3$ rotations	X/2,　Y/2
	X/2,　-Y/2
	-X/2,　Y/2
	-X/2,　-Y/2
	Y/2,　X/2
	Y/2,　-X/2
	-Y/2,　X/2
	-Y/2,　-X/2
$\pi/2$ rotations	X/2
	-X/2
	Y/2
	-Y/2
	-X/2,　Y/2,　X/2
	-X/2,　-Y/2,　X/2
Hadamard-like	X,　Y/2
	X,　-Y/2
	Y,　X/2
	Y,　-X/2
	X/2,　Y/2,　X/2
	-X/2,　Y/2,　-X/2

The CNOT-like class has $24^2 \times 3^2 = 5184$ elements.
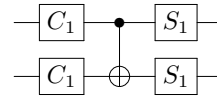
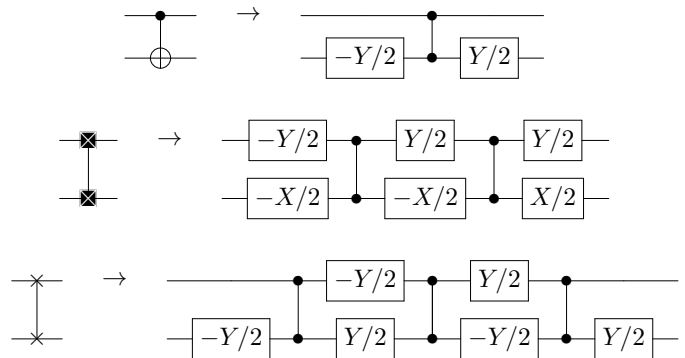The iSWAP-like class also has 5184 elements,
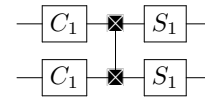
Finally the SWAP-like class, with 576 elements, is given by

bringing the full size of the two-qubit Clifford group to 11520. An approach using a reduced set of gates was used in Ref. [14].

Here, we rewrite the two-qubit Cliffords in terms of the CZ entangling gate. We rewrite the CNOT, iSWAP and SWAP in terms of the CZ:

As the single qubit gates preceeding the entangling operation (CZ gate) can be absorbed into C_1, and the final single qubit gates can be absorbed into S_1 (see Table S7), we have for the CNOT-like class,
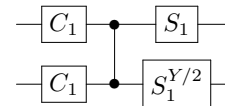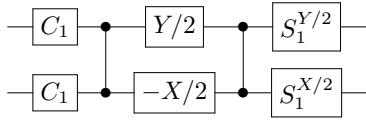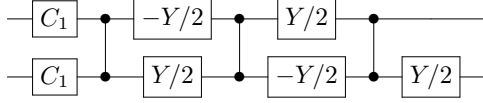

TABLE S7: The S_1 sets written in terms of physical gates in time; these are elements of the single qubit Clifford group, and therefore physically implemented in the same way.

S_1	I
	Y/2,　X/2
	-X/2,　-Y/2
$S_1^{X/2}$	X/2
	X/2,　Y/2,　X/2
	-Y/2
$S_1^{Y/2}$	Y/2
	Y,　X/2
	-X/2,　-Y/2,　X/2

the iSWAP-like class,

and the SWAP-like class,

The average number of gates for C_2 is 1.5 CZ gates and 8.25 single qubit gates. For the idle, we wait as long as the shortest single qubit gate. For a single qubit gate time of 20 ns and a CZ gate time of 40 ns, the average duration of C_1 is 37.5 ns, and C_2 is 160 ns.

The Clifford group is a 2-design. A set of unitaries $\{U_k\}_{k=1}^K$ is a 2-design if and only if [15]

$$\sum_{k,k'=1}^{K} |\text{Tr}\left(U_{k'}^\dagger U_k\right)|^4/K^2 = 2. \qquad (S2)$$

As a consistency check, we have verified that the single and two-qubit Cliffords we generate are indeed a 2-design with the above equation.

ESTIMATING THE ERROR PER CLIFFORD

Here, we connect the error per Clifford r to the errors of the single and two-qubit gates, measured when performing randomised benchmarking. This shows the physical significance of the error per Clifford, and is an important self-consistency check. We can give an estimate for the error per Clifford by determining the average number of single and two-qubit gates that go into a Clifford, combined with the single and two-qubit gate fidelities that we measure using interleaved randomised benchmarking. We assume that gate errors are small and uncorrelated, such that adding error when composing gates is a good approximation.

Single qubit Clifford group C_1

There are 45 single qubit gates used across 24 Cliffords. With the assumption that all single gates have the same error, the average error per Clifford is

$$r_{C_1} = 1.875 r_{\text{SQ}}, \qquad (S3)$$

with r_{SQ} the average single-qubit gate error.

Two qubit Clifford group C_2

The four classes of two-qubit Cliffords are composed from the two-qubit CZ gate, and the single-qubit gate sets C_1, S_1, $S_1^{Y/2}$, and $S_1^{X/2}$. The respective errors are given by: $r_{S_1} = 5r_{\text{SQ}}/3$, $r_{S_1^{X/2}} = 5r_{\text{SQ}}/3$, $r_{S_1^{Y/2}} = 2r_{\text{SQ}}$.

We now derive the average gate composition for the two-qubit Cliffords. For the single-qubit class:

$$r_{C_1 \otimes C_1} = \frac{90}{24} r_{\text{SQ}}. \qquad (S4)$$

CNOT-like class:

$$r_{\text{CNOT}} = r_{\text{CZ}} + \frac{89}{12} r_{\text{SQ}}. \qquad (S5)$$

iSWAP-like class:

$$r_{\text{iSWAP}} = 2r_{\text{CZ}} + \frac{113}{12} r_{\text{SQ}}. \qquad (S6)$$

SWAP-like class:

$$r_{\text{SWAP}} = 3r_{\text{CZ}} + \frac{35}{4} r_{\text{SQ}}. \qquad (S7)$$

The error per Clifford for C_2 is then given by

$$r_{C_2} = \frac{576}{11520} r_{C_1 \otimes C_1} + \frac{5184}{11520} r_{\text{CNOT}} + \qquad (S8)$$

$$\frac{5184}{11520} r_{\text{iSWAP}} + \frac{576}{11520} r_{\text{SWAP}} \qquad (S9)$$

$$= \frac{3}{2} r_{\text{CZ}} + \frac{33}{4} r_{\text{SQ}}. \qquad (S10)$$

And the error per two-qubit Cliffords interleaved with a CZ is

$$r_{C_2+\text{CZ}} = \frac{5}{2} r_{\text{CZ}} + \frac{33}{4} r_{\text{SQ}}. \qquad (S11)$$

Comparison to Experiment

Using these simple formulas, we find that our randomised benchmarking data are self-consistent. Using reasonable values of 0.001 and 0.006 for the single and two-qubit gates respectively, we calculate $r_{C_2} = 0.0173$, which is close to the experimental value of $r_{\text{ref}} = 0.0189$ in Fig. 3 in the main Letter; for the interleaved case the calculated value of $r_{C_2+\text{CZ}} = 0.0233$ is close to the experimental value of 0.0244 as well.

$N = 5$ GHZ STATE PULSE SEQUENCE

The pulse sequence for the algorithm to construct the five qubit GHZ state is shown in Fig. S8a. We use Hahn spin echoes on idling elements to suppress slow dephasing ($T_{\phi,2}$). The frequency diagram for the qubits is shown in Fig. S8b. Nearest neighbour qubits are detuned by 0.7 to 1.5 GHz, next-nearest neighbours are detuned by 0.4 to 0.5 GHz.
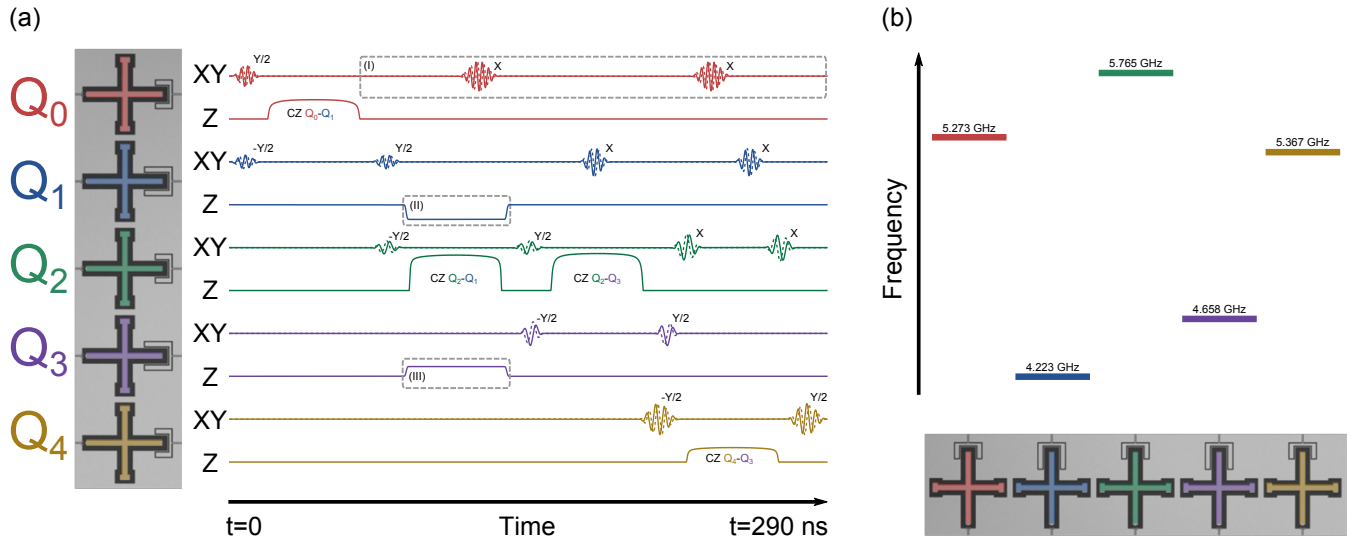
FIG. S8: **Pulse sequence for generating the** $N = 5$ **GHZ state and frequency diagram.** (a) The control signals for all five qubits. The algorithm consists of a Y/2 pulse on Q_0 followed by successive CNOT gates (implemented here with a CZ gate and -Y/2, Y/2 gates applied to the target) on each progressive pair of qubits in the array. The highlighted region (I) shows Hahn spin echo pulses X applied to Q_0 to suppress dephasing while idling. Spin echo pulses are also applied to Q_1 and Q_2. (II) We detune Q_1 to bring it closer in frequency to Q_2 for the CZ gate. (III) Simultaneously with the Q_1-Q_2 entangling operation, we detune Q_3 away to allow for selective entanglement. (b) The frequency diagram shows the idling frequencies for all qubits, and is one of the operating modes of the quantum processor.
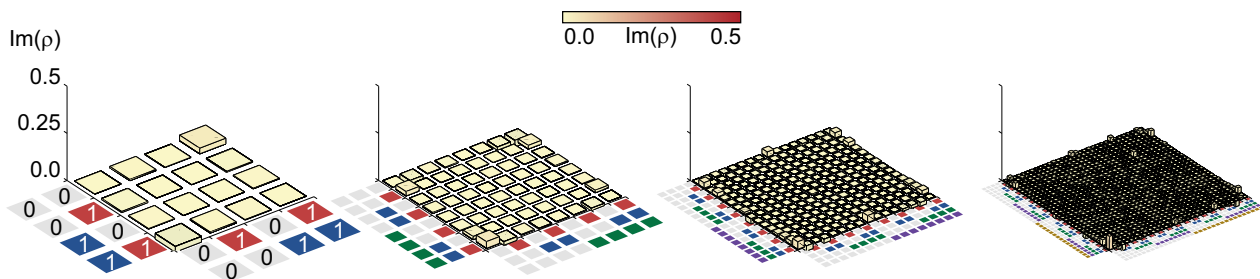

FIG. S9: **Quantum state tomography of the GHZ states: Imaginary parts.** Imaginary parts of the density matrices ρ for the $N = 2$ Bell state and the $N = 3, 4$ and 5 GHZ states. For clarity, the same scale as for the main Letter is used. $|\text{Im}\rho|$ is below 0.03, 0.04, 0.04 and 0.07 for $N = 2$ to 5, respectively.

QUANTUM STATE TOMOGRAPHY

The density matrices of the $N = 2$ Bell and $N = 3, 4, 5$ GHZ states are characterised using quantum state tomography. After state preparation, gates from $\{$ I, X/2, Y/2, X $\}^{\otimes N}$ are applied; with the measured probabilities the state can then be reconstructed. We use quadratic maximum likelihood estimation, using the MATLAB packages SeDuMi and YALMIP, to extract the density matrix while constraining it to be Hermitian, unit trace, and positive semidefinite; the estimation is overconstrained. Non-idealities in measurement and state preparation are suppressed by performing tomography on a zero-time idle [16, 17]. We note that tomography is only "as good as" the

tomography pulses, which have an average fidelity above 0.999. Fidelities and uncertainties correspond to the mean and standard deviation of 10 measurements, consisting of 10^4 ($N = 2, 3$) or $6 \cdot 10^3$ ($N = 4, 5$) repetitions each. The density matrices plotted in the main Letter are constructed by averaging all measured probabilites, effectively using 10^5 ($N = 2, 3$) or $6 \cdot 10^4$ ($N = 4, 5$) repetitions.

The imaginary part of the density matrices (ρ) is plotted in Fig. S9. The Pauli operator representation is shown in Fig. S10.

---

* These authors contributed equally to this work

[1] Barends, R. *et al.* Coherent Josephson qubit suitable for scalable quantum integrated circuits. *Phys. Rev. Lett.* **111**, 080502 (2013).

[2] Chen, Z. *et al.* Fabrication and Characterization of Aluminum Airbridges for Superconducting Microwave Circuits. arXiv:1310.2325.

[3] Megrant A. *et al.* Planar Superconducting Resonators with Internal Quality Factors above One Million. *Appl. Phys. Lett.* **100**, 113510 (2012).

[4] Mutus, J. *et al.* Strong environmental coupling in a Josephson parametric amplifier. arXiv:1401.3799.

[5] Kelly, J. *et al.* Optimal quantum control using randomized benchmarking. arXiv:1403.0035.

[6] Fowler, A. G., Martinis, J. M. Quantifying the effects of local many-qubit errors and non-local two-qubit errors on topological codes. arXiv:1401.2466.

[7] Fowler, A. G., Mariantoni, M., Martinis, J. M., & Cleland, A. N. Surface codes: Towards practical large-scale quantum computation. *Phys. Rev. A* **86**, 03232 (2012).

[8] Fowler, A. G. Coping with qubit leakage in topological codes. *Phys. Rev. A* **88**, 042308 (2013).

[9] Jeffrey, E. *et al.* Fast Scalable State Measurement with Superconducting Qubits. arXiv:1401.0257.

[10] Fowler, A. G. Optimal complexity correction of correlated errors in the surface code. arXiv:1310.0863.

[11] Lucero E. *et al.* Reduced phase error through optimized control of a superconducting qubit. *Phys. Rev. A* **82**, 042339 (2010).

[12] Gambetta J. M. *et al.* Characterization of addressability by simultaneous randomized benchmarking. *Phys. Rev. Lett.* **109**, 240504 (2012).

[13] Córcoles, A. D. *et al.* Process verification of two-qubit quantum gates by randomized benchmarking. *Phys. Rev. A* **87**, 030301. (2013).

[14] Gaebler, J. P. *et al.* Randomized Benchmarking of Multiqubit Gates *Phys. Rev. Lett.* **108**, 260503 (2012).

[15] Gross D., Audenaert K., & Eisert J. Evenly distributed unitaries: On the structure of unitary designs. *J. Math. Phys.* **48**, 052104 (2007).

[16] DiCarlo, L. *et al.* Preparation and measurement of three-qubit entanglement in a superconducting circuit. *Nature* **467**, 574-578 (2010).

[17] Neeley, M. *et al.* Generation of three-qubit entangled states using superconducting phase qubits. *Nature* **467**, 570-573 (2010).
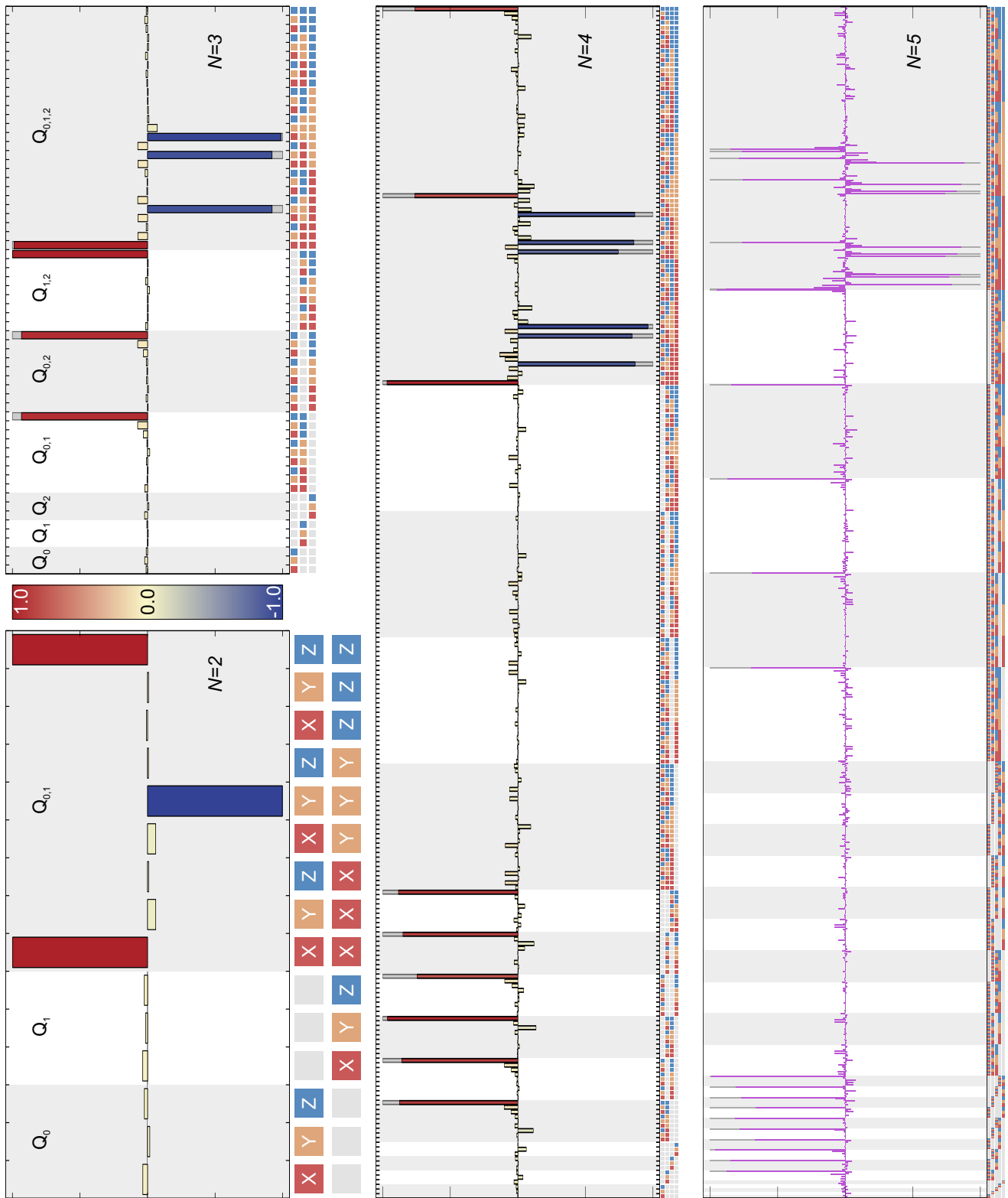
FIG. S10: **Pauli operator representation for the** $N = 2$ **Bell state and the** $N = 3, 4$ **and** 5 **GHZ states.** The bars show expectation values of combinations of Pauli operators, ideal in grey, experimental values in colour. Apart from the trivial even number Z-correlations, the data show significant elements only for the largest correlations.